Cell Reports
Physical Science

CellPress
OPEN ACCESS

Article

Modular polyoxometalate-intercalated layered double hydroxide membranes for molecular sieving and *in situ* regeneration

Wan-Lei Zhao,[1] Yubing Liu,[1] Yixin Yang,[1] Wei Chen,[1,*] Haralampos N. Miras,[2,*] and Yu-Fei Song[1,3,*]

SUMMARY

The design and synthesis of two-dimensional membranes with ultrahigh permeability, selectivity, and antifouling properties have been a significant challenge. Herein, we propose a facile approach to design modular polyoxometalate-intercalated layered double hydroxide membranes using a charge-driven self-assembly process. The resultant MgAl-SiW_{12} membrane shows 4 times higher water permeance (>130 L m^{-2} h^{-1} bar^{-1}) than that of its MgAl-NO_3 precursor. Excellent retention of >99% for Congo red and Evans blue is achieved by the MgAl-SiW_{12} membrane, which can be regenerated (permeance recovery > 95%) via a simple UV-vis irradiation cycle. Insertion of the SiW_{12} cluster into layered double hydroxide allows precise control and modulation of the interlayer's spacing and hydrophilicity and promotes spontaneous electron migration and interfacial charge carrier separation. Moreover, the ·OH and $\cdot O_2^-$ radicals forming during the irradiation process are responsible for the degradation of contaminants.

INTRODUCTION

Nanofiltration technology based on size sieving and charge repulsion has received attention from academia and industry as an advanced molecular separation technique. With the advantages of low energy consumption, high efficiency, and space saving, nanofiltration has played an important role in the field of water treatment.[1] Recently, two-dimensional (2D) lamellar membranes have emerged as competitive candidates for gas or liquid separation due to their unique ultrathin architecture and adjustable nanometer/sub-nanometer interlayer channels. Two-dimensional materials, such as graphene and its derivatives,[2] hexagonal boron nitride (BN),[3] covalent organic frameworks (COFs),[4–6] transition-metal carbides/carbonitrides (MXenes),[7,8] and layered double hydroxides (LDHs),[9,10] have attracted attention as promising building block candidates for the construction of new molecular separation membranes. This was due to their inherent structural features that allowed the transport of small molecules and ions across the lamellar membranes through their intrinsic pores and nanochannels between adjacent layers. Unfortunately, the permeation rate of water molecules in the narrow two-dimensional channels formed by the tightly stacked nanosheets was very low. Researchers have improved the transport behavior of water molecules by modulating the interlayer distance as well as the chemical environment, generally via intercalation of zero-dimensional (0D) nanodots,[11,12] one-dimensional (1D) nanowires,[13] 2D nanosheets[14] into 2D materials. However, uncontrollable intercalation led to trade-offs between permeability and selectivity. Additionally, continuous operation of nanofiltration membranes can lead to passivation on the membranes surface, resulting in blocked transport

[1]State Key Laboratory of Chemical Resource Engineering, Beijing University of Chemical Technology, Beijing 100029, China

[2]School of Chemistry, University of Glasgow, Glasgow G12 8QQ, UK

[3]Lead contact

*Correspondence: chenw@mail.buct.edu.cn (W.C.), charalampos.moiras@glasgow.ac.uk (H.N.M.), songyf@mail.buct.edu.cn (Y.-F.S.)

https://doi.org/10.1016/j.xcrp.2022.101189

channels and increased mass transfer resistance. Consequently, it was of fundamental importance to explore a new design approach for the construction of highly efficient 2D membranes with modular interlayer channel microstructures for bespoke applications.

LDHs, with the molecular formula $[M^{2+}_{1-x}M^{3+}_{x}(OH)_2](A^{n-})_{x/n}\cdot mH_2O$, consist of a positively charged laminate and intercalated guest anions between layers. Exfoliated LDH nanosheets show the advantages of thin layer thickness, large specific surface area, and surface modifiability, which are ideal candidates for the preparation of 2D membranes. As a typical class of 2D supramolecular layered materials with moderate rigidity, LDHs have received increasing attention in the field of gas and liquid separation.[15,16] LDHs exhibit uniform interlayer galleries and the interlayer spacing can be adjusted by intercalating different charge compensating anions. Moreover, LDH layers possess high charge density and uniform charge distribution, which can induce the orientation alignment of the guest molecules.[17,18] Finally, LDHs are inexpensive, easily available, and environmentally benign 2D materials with various industrial applications.[19]

Polyoxometalates (POMs) are a group of metal oxides, such as V, Mo, and W, and POMs possess well-defined chemical composition and molecular structures.[20–23] In addition, POMs show adjustable Lewis acidity and wide range of redox properties.[24–28] In recent years, Song et al. reported a number of POM-intercalated LDH systems with excellent performance in catalytic reactions.[29–32] POMs were restricted to the flexible interlayer region of LDH so that the catalytic active sites were uniformly distributed in the interlayer arrangement of LDH, thus improving its catalytic activity and selectivity.[33–35] Moreover, because of their unique chemical composition and electronic structure, POMs exhibited excellent photochemical properties under various experimental conditions.[36] Keggin structured POMs are a class of sphere-like discrete clusters with T_d symmetry. The electrons and holes generated by the photoexcited oxygen-to-metal charge transfer endowed it excellent photocatalytic performance and it was one of the most explored POMs in the field of photocatalysis.[37,38] On the basis of the uniform nature and tunability of the interlayer galleries of LDHs, as well as the precise size and unique electronic structure of POMs, the intercalation of POMs into LDHs may present a route to an efficient 2D membrane.

Herein, we demonstrated a facile design approach for the charge-driven self-assembly of negatively charged SiW_{12} clusters (~9 Å) into LDH nanosheets, followed by deposition onto hydrolyzed polyacrylonitrile (PAN) support under vacuum-assisted filtration. This new design approach exhibited the following advantages: (1) the rigid Keggin structured SiW_{12} clusters had uniform size at the nanoscale, allowing precise control of the interlayer spacing of the LDH; (2) the hydrophilic nature of the SiW_{12} clusters altered the channel's microenvironment, inducing ordered alignment of water molecules and promoting rapid transport of water molecules; and (3) the incorporated SiW_{12} clusters induced an accelerated charge transfer and interfacial charge carrier separation, resulting in remarkable photocatalytic *in situ* cleaning capability.

RESULTS AND DISCUSSION

Microstructure and morphology of MgAl-SiW_{12} laminates

Figure 1A demonstrates the synthetic procedure of the MgAl-SiW_{12} membrane. The solution of SiW_{12} was slowly added into the suspension of positively charged MgAl-LDH nanosheets, and they were reconstituted into MgAl-SiW_{12} laminates.

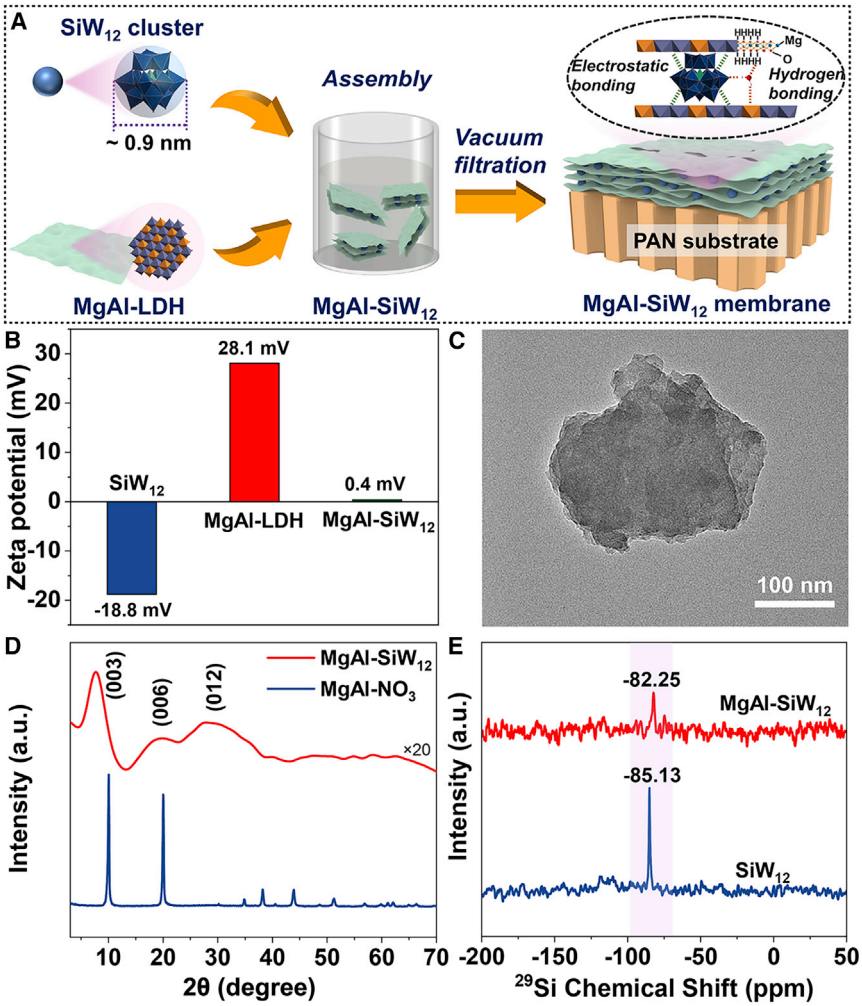

Figure 1. Characterization of structure and morphology of MgAl-SiW$_{12}$ laminates

(A) Illustration of the assembly and interactions of SiW$_{12}$ and MgAl-LDH nanosheets.

(B) Zeta potentials of SiW$_{12}$, MgAl-LDH and MgAl-SiW$_{12}$ laminates.

(C) TEM image of MgAl-SiW$_{12}$ laminates. Scale bar, 100 nm.

(D) XRD patterns of MgAl-SiW$_{12}$ and MgAl-NO$_3$.

(E) ^{29}Si MAS NMR spectra of SiW$_{12}$ and MgAl-SiW$_{12}$ laminates.

The MgAl-SiW$_{12}$ laminates were then deposited on the hydrolyzed PAN support driven by vacuum filtration. Electrostatic and hydrogen bonding interactions induced the assembly of LDH with SiW$_{12}$. As the building blocks of 2D nanochannels, monolayer LDH nanosheets were obtained by exfoliating bulk LDH in formamide (Figures S1–S7). The zeta potential of the positively charged MgAl-LDH nanosheets suspension were found to be 28.1 mV, and that of the negatively charged SiW$_{12}$ solution was −18.8 mV (Figure 1B). When MgAl-LDH and SiW$_{12}$ were assembled in solution, the zeta potential was found to be approximately zero. The visible laser light beam in the MgAl-SiW$_{12}$ laminates suspension demonstrated the Tyndall light scattering effect (Figure S8). Transmission electron microscopy (TEM) imaging indicated a well-ordered assembly of MgAl-SiW$_{12}$ laminates (Figure 1C). Dynamic light scattering (DLS) showed that the average lateral size of MgAl-SiW$_{12}$ nanosheets was about 390 nm (Figure S9). Powder X-ray diffraction (XRD) of MgAl-SiW$_{12}$ laminates exhibited an enlarged d-spacing value of 1.37 nm compared with the original

MgAl-NO_3 d-spacing value of 0.743 nm (Figure 1D).[31,32] Subtracting the theoretical thickness of the monolayer LDH nanosheets of 0.48 nm, the height among the laminates was calculated to be 0.89 nm.[39] Fourier transform infrared (FTIR) spectra of the MgAl-SiW_{12} exhibited strong absorption bands located at 1,010, 964, 915, and 790 cm^{-1} (Figure S10), which can be assigned to the characteristic vibrational peaks of O–Si, O–W, W–Ob_1–W and W–Ob_2–W, respectively.[40] Meanwhile, the peak of NO_3^- in MgAl-SiW_{12} became much weaker.[41] The ^{29}Si MAS nuclear magnetic resonance (NMR) spectra of SiW_{12} and MgAl-SiW_{12} showed peaks centered at −85.13 and −82.25 ppm, respectively (Figure 1E). Such small shift was due to the interaction between SiW_{12} and MgAl-LDH.[42]

Characteristics of MgAl-SiW_{12} membranes

The observed FTIR peaks of the MgAl-SiW_{12} membrane, found be at 1,010, 964, 915, and 790 cm^{-1} and corresponded to the intercalated SiW_{12} cluster (Figure S11). Top-view scanning electron microscopy (SEM) images (Figures S13B and 2A) of the MgAl-NO_3 and MgAl-SiW_{12} membranes revealed a fairly smooth and flat surface without any visible defects or cracks. When the initial amount of MgAl-LDH used was 2.4 mg, the thickness of the obtained MgAl-NO_3 layer was found to be approximately 410 nm, while the thickness of the MgAl-SiW_{12} membrane was 450 nm (Figures S13A and 2B). The cross-sectional SEM image of thick MgAl-SiW_{12} membrane displayed a typical laminate structure, indicating a well-stacked interlayer channel (Figure 2C). The thickness of the selective layer can be easily adjusted by altering the amount of MgAl-SiW_{12} (Figure S14). Close inspection of the high-resolution TEM (HRTEM) image of the MgAl-SiW_{12} membrane, revealed a number of highly dispersed black dots with a diameter of $\approx$1 nm which correspond to the size of the intercalated SiW_{12} nanoclusters (Figure 2D). Inductively coupled plasma optical emission spectrometry (ICP-OES) results indicated that the loading of SiW_{12} was about 53%. Energy dispersive spectrometry (EDS) mapping of the selected elements showed a homogeneous distribution in both membrane surface and cross section (Figures S15 and S16). From the cross-sectional EDS elemental analyses of the MgAl-SiW_{12} membrane, it can be seen that the elements Mg, Al, Si and W were present mainly in the selective layer (Figure S17). The surface roughness of the MgAl-NO_3 membrane can be found to be higher (45.9 nm) than that of MgAl-SiW_{12} membrane (28.4 nm), which can be attributed to the disordered accumulation of nanosheets (Figure S18). This observation indicated that the SiW_{12} cluster acted as template that induced a regular self-organized structure of the selective layer.

Variation in the d-spacing of membranes was of vital importance for selective molecular separation and transport performance. Except for three major diffractions of the hydrolyzed PAN substrate, the peak located at 2θ of 7.46° was the diffraction of (003) peak of MgAl-NO_3 membrane which indicated a d-spacing of 1.18 nm on the basis of Bragg's law (Figure 2E).[43–45] The enlarged interlayer spacing of MgAl-NO_3 membrane compared with that of MgAl-NO_3 platelets was due to the accompanying water and residual formamide molecules along with the intercalated NO_3^-, which was consistent with previous reports.[46] The peak centered at 2θ of 6.90° was the diffraction of (003) peak of MgAl-SiW_{12} membrane which was indicative of 1.37 nm d-spacing. The gallery height value of the MgAl-SiW_{12} membrane was estimated to be 0.89 nm, which was highly beneficial to rapid molecular transportation. The X-ray photoelectron spectroscopy (XPS) study revealed that the binding energy of W 4f exhibited a negative shift, which can be attributed to the strong interaction between MgAl-LDH and SiW_{12} clusters (Figure S19). Moreover, the Mg 1s and Al 2p spectra of MgAl-SiW_{12} showed a small shift compared with the MgAl-NO_3 samples,

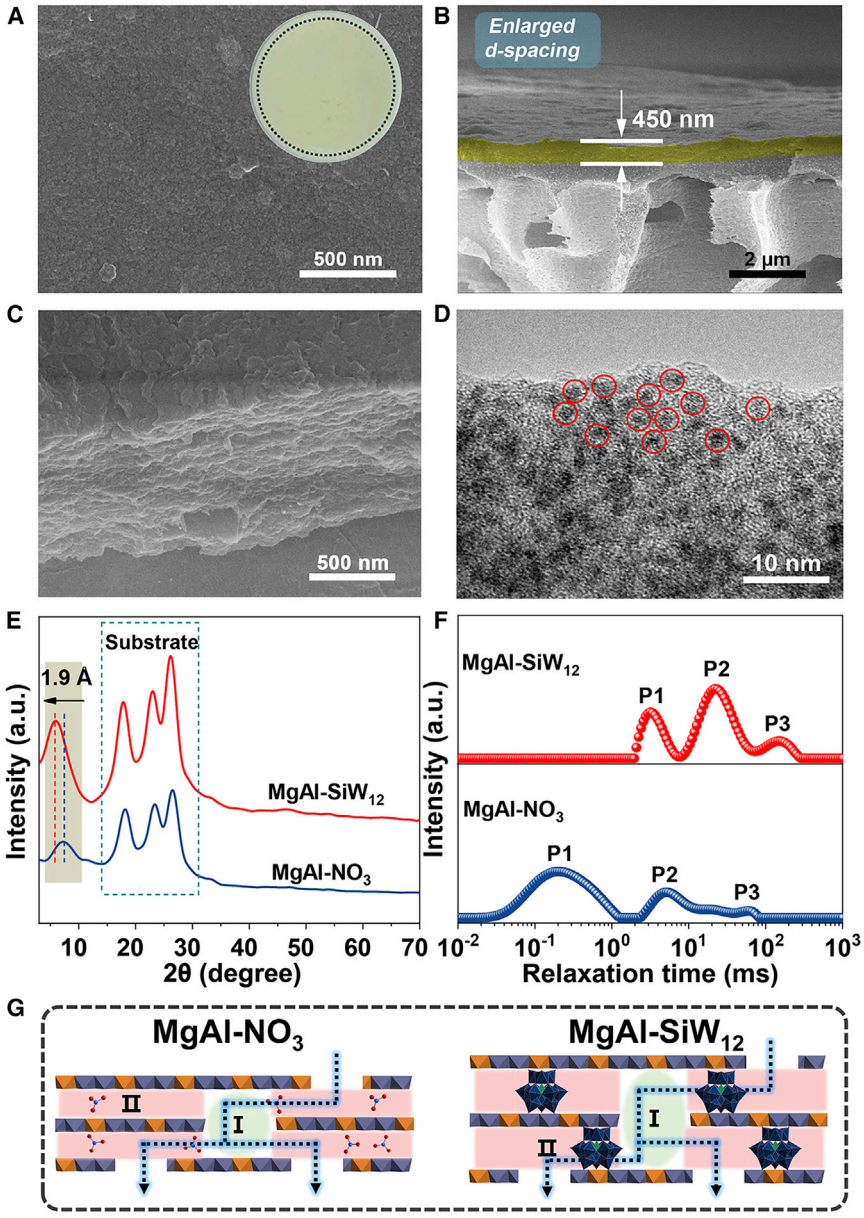

Figure 2. Characteristics of MgAl-SiW$_{12}$ membranes

(A and B) SEM images of top view (A) and cross-section (B) of MgAl-SiW$_{12}$ membranes. Scale bars, 500 nm (A) and 2 μm (B).

(C and D) Cross-sectional SEM (C) and HRTEM images (D) of thick freestanding MgAl-SiW$_{12}$ membranes. Scale bars, 500 nm (C) and 10 nm (D).

(E–G) XRD patterns (E), low-field NMR spectra (F), and schematic illustration (G) of confinement space of the MgAl-NO$_3$ and MgAl-SiW$_{12}$ membranes, respectively.

which can be attributed to the strong electrostatic interaction with the SiW$_{12}$ clusters.[47]

Brunauer-Emmett-Teller (BET) and low-field NMR (LF-NMR) techniques were used to explore changes in the microstructure of nanochannels.[48] BET showed an increase in the specific surface area of MgAl-SiW$_{12}$ (28.6 m^2/g) compared with MgAl-NO$_3$ (4.9 m^2/g) (Figure S20). Low-field NMR worked by determining the relaxation time (T_2)

on the basis of the process of energy exchange between hydrogen atoms and other atoms, and the position of T_2 represented the different states of the bound hydrogen atoms. Hydrogen atoms that were less bound had high degrees of freedom and long relaxation time, which implied larger pore sizes. Three peaks appeared in the region of 10^{-2}–10^{3} ms (Figure 2F). In the case of the MgAl-NO_3 membrane, only a single population existed in the sub-nanometer-confined domain (0.8–1 ms) (region Ⅱ in Figure 2G). The peak P2 and P3 (2–100 ms) represented water molecules between the in-plane nanosheet slits (region I in Figure 2G). Following the intercalation of the SiW_{12} cluster, the relaxation time (T_2) of the sub-nanometer-confined water increased from 0.2 to 3.3 ms. Meanwhile, the remaining two peaks P2 and P3 shifted from 5 to 60 ms to 22 and 151 ms, respectively. In combination with the XRD data, we can conclude that the increased T_2 relaxation time of MgAl-SiW_{12} membrane was the result of the increased d-spacing following the intercalation of the SiW_{12} cluster.

Separation performance of MgAl-SiW_{12} membranes

The used PAN substrate was negatively charged at −60.51 mV because of the partial hydrolysis of –CN to –COOH on the surface (Figures S12 and S21). When deposition of MgAl-NO_3 or MgAl-SiW_{12} onto the partially hydrolyzed PAN, the resulting MgAl-NO_3 membranes and MgAl-SiW_{12} membranes showed the zeta potential of −21.87 and −35.39 mV, respectively (Figure S21). The interfacial interactions including the electrostatic and hydrogen bonding interactions between LDH and the hydrolyzed PAN substrate ensured that selective layer would not be stripped from the substrate of PAN.

The separation performance of the MgAl-SiW_{12} membranes was evaluated by filtering Congo red (CR) solution. The water permeance kept decreasing as a function of selective layer's thickness (Figure 3A), indicating that the thicker MgAl-SiW_{12} layer led to higher resistance to water permeation. For example, the permeance decreased from 814.26 ± 18.64 to 93.24 ± 0.30 L m^{-2} h^{-1} bar^{-1}, whereas the CR rejection rate improved from 14.81% ± 2.59% to 99.22% ± 0.74%. To evaluate its stability, the MgAl-SiW_{12} membranes were kept immersed in water for seven days, and XRD did not reveal significant changes, indicating good stability of the membranes (Figure S22). Moreover, the separation performance of the MgAl-NO_3 and MgAl-SiW_{12} membrane are compared in Figure 3B. The permeance of MgAl-SiW_{12} membranes can be found to be 4 times higher than that of the MgAl-NO_3 membranes. Higher water permeance was associated with the enlarged interlayer spacing between LDH host layers, as illustrated by the XRD and LF-NMR data. As shown in Figure 3C, the flux of MgAl-SiW_{12} membranes increased linearly, indicating that the accessibility interlayer channels of the membrane were not disrupted. This demonstrated a remarkably enhanced pressure resistance compared with the MgAl-NO_3 membranes. The obtained MgAl-SiW_{12} membranes exhibited significantly higher permeance and rejection rates compared with other membranes reported in the literature (Figure 3D; Table S2).

The molecular dynamics (MD) simulations were used to explore the transport behavior of water molecules in MgAl-SiW_{12} nanostructures. The results showed that the higher interaction energy (−3378.43 kcal mol^{-1}) between the nanochannels of MgAl-SiW_{12} and water molecules enabled the movement of water molecules to be restricted, further reducing the collision frequency between them (Figure S23). As a result, the water molecules formed an ordered transport layer parallel to the laminate in regular nanochannels. Figures 3E and 3F simulated the mean square distance (MSD) and the diffusion coefficient of water molecules in the nanochannel to investigate the influence of interlayer spacing and chemical environment on water

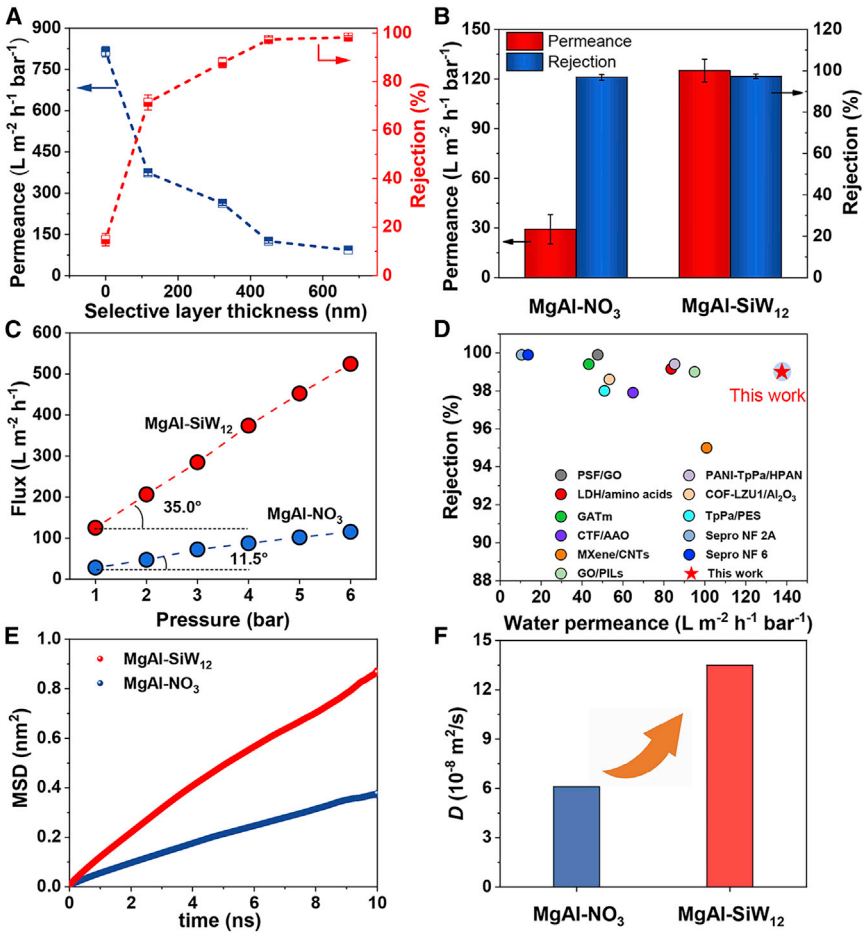

Figure 3. Separation performance of MgAl-SiW_{12} membranes

(A) Separation performance optimization of MgAl-SiW_{12} membrane as a function of selective layer thickness. The average permeance and rejection data are presented; error bars represent the standard error of three membranes.

(B) Separation performance of MgAl-NO_3 and MgAl-SiW_{12} membranes. The average permeance and rejection data are presented; error bars represent the standard error of three membranes.

(C) Relation between water flux and operating pressure for MgAl-NO_3 and MgAl-SiW_{12} membranes.

(D) Comparison of MgAl-SiW_{12} membrane with the reported separation membranes.

(E and F) Mean square distance (E) and diffusion coefficient (F) of water in the nanochannel.

diffusion behavior. The slope of the curve reflected the rate of penetration of water molecules in the channels.[49] The slope of the curve and diffusion coefficient of MgAl-SiW_{12} were larger than the one observed in MgAl-NO_3, which was due mainly to the high affinity of SiW_{12} clusters for water molecules and the increased d-spacing. MgAl-SiW_{12} possessed the faster transport rate for water molecules, resulting in high permeance. Hence, molecular dynamics simulations were in good agreement with the experimental observations.

As a proof of concept, we used dye molecules as example to evaluate the separation performance of membranes. The used dyes herein were repulsive in approximately the order of their molecular weight (MW) (Figure 4A; Table S1). CR, Evans blue (EB), and methyl blue (MB) with higher molecular weights exhibited higher rejection rates (>97%), while low-molecular weight methyl orange (MO) exhibited only a rejection of

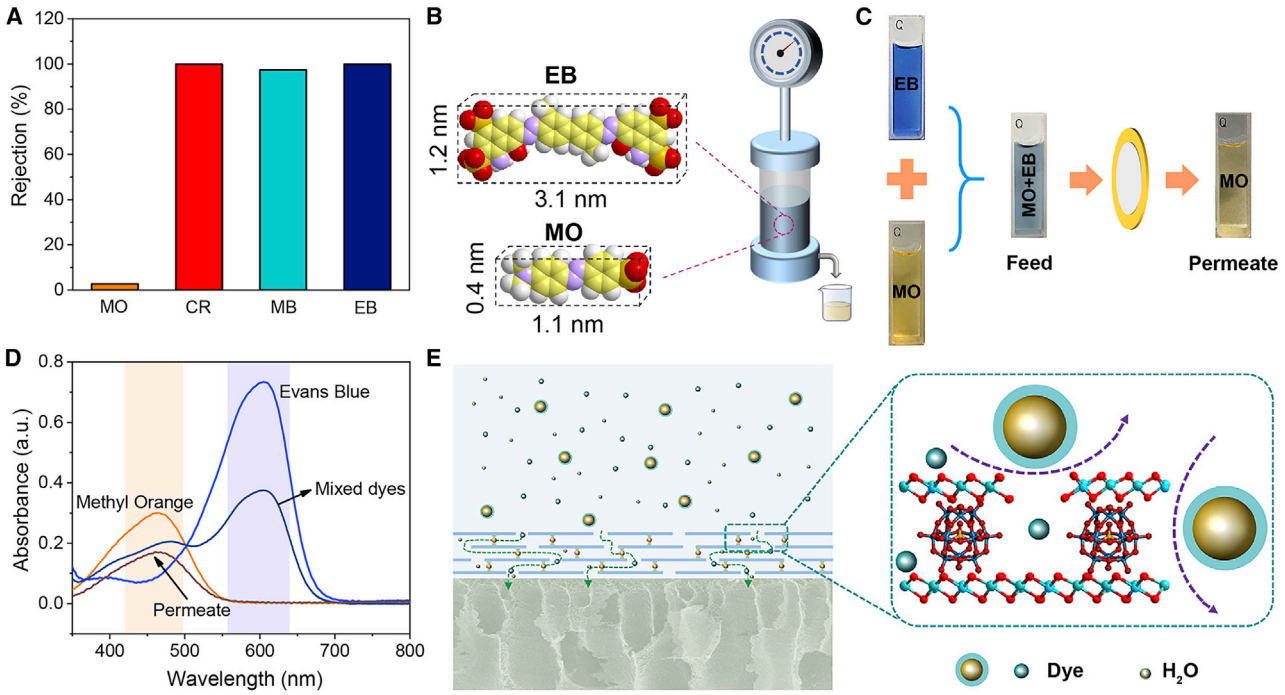

Figure 4. Accurate sieving on the basis of molecular size

(A) Dye rejections of MgAl-SiW_{12} membranes as a function of molecular weight of dyes.

(B and C) Precise molecular separation of MO (327.33 g/mol) from EB (960.79 g/mol) in water.

(D) UV-vis absorbance spectra of the feed, the permeate and the retentate.

(E) Illustration of molecular transport through MgAl-SiW_{12} membrane channels.

2.7% (Figure S24). The adsorption capacity of MgAl-SiW_{12} membranes for CR and MO were found to be 9.20% and 1.17%, respectively (Figure S25), suggesting the low adsorption capacity for negatively charged dyes. The dynamic adsorption experiments showed that the adsorption capacity of CR and EB were approximately 5.9% and 8.9% (Figure S26). Thus, we can safely rule out the possibility that the observed dye separation might be due to adsorption.

In an effort to demonstrate the membrane's ability for accurate molecular sieving, we carried out separation experiments in the presence of a mixture of EB (blue) and MO (yellow) (Figure 4B). The MO molecules can pass easily through the membrane, while the EB remained in the feed solution (Figure 4C). In addition, UV-vis spectra of the dye solution can further confirm that the larger sized EB was completely rejected and only the absorption peak of MO was present in the permeate (Figure 4D). As such, the nanochannels within the membrane facilitated the selective sieving of dye molecules on the basis of their size and shape (Figure 4E).

Photocatalytic *in situ* cleaning performance

The long-term stability of the membrane in separation processes was a huge challenge specifically in aqueous media. The membranes were tested in pure water for 8 h continuously. The permeance declined from 40.31 to 137.66 to 33.99 and 122.68 L m^{-2} h^{-1} bar^{-1} (Figure 5A), which corresponded to declines of 15.67% and 10.88% for MgAl-NO_3 and MgAl-SiW_{12}, respectively (Figure 5B). Under continuous-flow filtration conditions, the SiW_{12} components acted as rigid pillars between LDH layers, introducing structural rigidity and minimizing layer compression. Under similar continuous running conditions for 8 h in the presence of CR as the feed

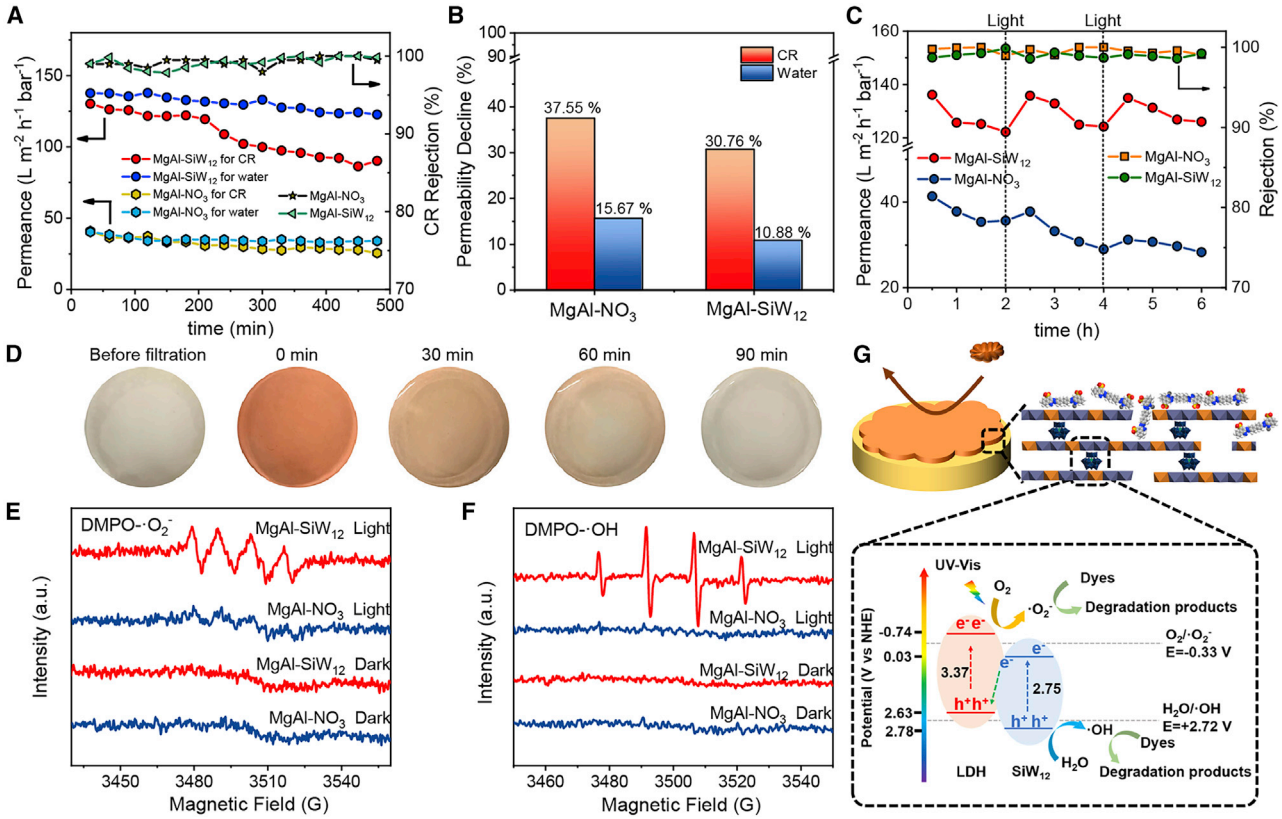

Figure 5. Photocatalytic *in situ* cleaning test

(A) Continuous test for CR and pure water.

(B) Permeability decline of the two membranes calculated from (A) after 8 h of operation.

(C) Permeance of the MgAl-NO_3 and MgAl-SiW_{12} membranes in separation-photocatalysis experiments for CR.

(D) Photography of the fouled MgAl-SiW_{12} membrane at different times under UV-vis irradiation.

(E and F) ESR spectra of DMPO-·O_2^- (E) and DMPO-·OH (F) adducts in the systems of MgAl-NO_3 and MgAl-SiW_{12} before and after irradiation.

(G) Proposed mechanism for photocatalytic degradation of pollutants on MgAl-SiW_{12} membrane under UV-vis irradiation.

solution, the permeability declined by 37.55% and 30.76% for MgAl-NO_3 and MgAl-SiW_{12}, respectively. The observed decline of the permeability can be attributed to dye molecule aggregation on the membrane's surface. After the first 2 h of continuous running conditions using a feed solution containing CR, the fouled MgAl-SiW_{12} membrane showed a decrease in permeance from 136.11 to 122.15 L m^{-2} h^{-1} bar^{-1}. The continuous-flow process was interrupted, and the fouled membrane was immersed in a small amount of aqueous solution followed by irradiation for 2 h using UV-vis light. The regenerated membrane was used in a 2nd round experiments, where its permeability can be recovered to nearly 100%, exhibiting very good reproducibility over three consecutive cycles (Figure 5C). In contrast, the MgAl-NO_3 membranes did not exhibit complete regeneration and restoration of their permeance under the same conditions (e.g., 91.34% and 82.69% recovery for MgAl-NO_3 membrane in the 2nd and 3rd rounds, respectively). In Figure 5D, we can visualize the gradual fading of the red color characteristic of the CR deposit when irradiated with UV-vis irradiation over 90 min. The FTIR spectra clearly showed the weakening of the C-S bond (1,059 cm^{-1}) in CR (Figure S27), while the membrane layer spacing remained unaltered after irradiation (Figure S28). Additional control experiments were conducted using only UV-vis light and only water as additional confirmation of the photocatalytic effect of MgAl-SiW_{12} (Figure S29).

UV-visible diffuse reflectance spectra of SiW_{12}, MgAl-NO_3 and MgAl-SiW_{12} were characterized to explore the photocatalytic mechanism of the MgAl-SiW_{12} membrane (Figure S30A). More specifically, the MgAl-SiW_{12} and MgAl-NO_3 composites exhibited absorption edges at 370 and 430 nm with bandgaps of 3.00 and 3.37 eV, respectively (Figure S30B). The lower bandgap of MgAl-SiW_{12} indicated its higher use of UV-vis light. The photocurrent density of MgAl-SiW_{12} was much higher than that of MgAl-NO_3, indicating that MgAl-SiW_{12} produced more electron-hole pairs under UV-vis irradiation (Figure S31A).[50] Significant reduction of photoluminescence (PL) signal for MgAl-SiW_{12} indicated that the intercalation structure can achieve efficient charge separation (Figure S31B).[51,52] As shown in Figure S31C, the MgAl-SiW_{12} (39.9 Ω) exhibited a smaller charge transfer resistance (R_{ct}) than MgAl-NO_3 (59.4 Ω), suggesting that MgAl-SiW_{12} had more efficient electron-hole separation and transfer.[53] The aforementioned results demonstrated the ability of the MgAl-SiW_{12} laminate to suppress the recombination of light-generated carriers, enabling the MgAl-SiW_{12} membrane to exhibit excellent photocatalytic performance. In an effort to understand the underlying photocatalytic mechanism, we aimed to identify the active species by means of electron spin resonance. In the absence of light, there was no measurable signal (Figures 5E and 5F) of the methanolic dispersion of MgAl-SW_{12} while under UV-vis irradiation, characteristic peaks with an intensity ratio of 1:1:1:1 for DMPO-$\cdot O_2^-$ can be detected (Figure 5E). Additionally, the characteristic peaks of DMPO-·OH radical with an intensity ratio of 1:2:2:1 can be detected in the aqueous dispersion of MgAl-SiW_{12} (Figure 5F).[54] On the basis of the obtained Mott-Schottky data for the MgAl-NO_3 and the flat-band potential of SiW_{12} measured by cyclic voltammetry, we estimated the relative positions of conduction band (CB) and valence band (VB) of MgAl-NO_3 and SiW_{12} (Figure S32). As illustrated in Figure 5G, a photocatalytic mechanism based on the degradation of contaminant by free radicals was revealed. The processes of active species generation and contaminant degradation can be described as follows:

$$MgAl-SiW_{12} + hv \rightarrow e_{CB}^- + h_{VB}^+ \quad \text{(Equation 1)}$$

$$O_2 + e_{CB}^- \rightarrow \cdot O_2^- \quad \text{(Equation 2)}$$

$$H_2O + h_{VB}^+ \rightarrow \cdot OH + H^+ \quad \text{(Equation 3)}$$

$$\cdot O_2^- + \textit{dye foulant} \rightarrow \textit{degraded products} \quad \text{(Equation 4)}$$

$$\cdot OH + \textit{dye foulant} \rightarrow \textit{degraded products} \quad \text{(Equation 5)}$$

After irradiation, the photogenerated electron-hole pairs were generated on MgAl-SiW_{12} membranes (Equation 1). The VB of LDH received the photogenerated electrons from the CB of SiW_{12} and recombined. Electrons left in the CB of LDH and holes left in the VB of SiW_{12} effectively prevented the recombination of electron-hole pairs. Afterward, oxygen was reduced by photogenerated electrons (Equation 2) and water was oxidized by photogenerated holes (Equation 3). Eventually, the generated $\cdot O_2^-$ and ·OH radicals were used to degrade dye molecules (Equations 4 and 5).[55]

In summary, we demonstrated a facile design for the construction of POM-intercalated LDH membranes following a charge-driven self-assembly approach. The internal nanochannels of MgAl-SiW_{12} membranes can be precisely modulated to 0.89 nm. High water permeance (>130 L m^{-2} h^{-1} bar^{-1}) and remarkable solute retention (>99% rejection to Congo red and Evans blue) can be achieved by the MgAl-SiW_{12} membranes, which can recover their permeance by more than 95%

over three cycles by employing a UV-vis irradiation regeneration process. The MD simulations revealed that the strong interactions between MgAl-SiW_{12} and water molecules induced an ordered organization of water molecules within the confined channels, forming transport layers parallel to the laminate in regular nanochannels. Moreover, incorporating SiW_{12} into MgAl-LDH can effectively decrease the electron-hole recombination rate and enhance the photocatalytic performance of the membrane. ESR experiments showed that the generation of $\cdot OH$ and $\cdot O_2^-$ radicals in the aqueous system promoted the rapid degradation of pollutants. This work paved the way for the preparation of high-performance 2D lamellar membranes with modular nanochannels and photocatalytic *in situ* self-cleaning and regeneration capabilities for various applications.

EXPERIMENTAL PROCEDURES

Resource availability

Lead contact

Further information and requests for resources and reagents should be directed to and will be fulfilled by the lead contact, Yu-Fei Song (email: songyf@mail.buct.edu.cn).

Materials availability

This study did not generate new unique reagents.

Data and code availability

The authors declare that the data supporting the findings of this study are available within the article and the supplemental information. All other data are available from the lead contact on reasonable request.

Chemicals and reagents

$MgCl_2 \cdot 6H_2O$, $AlCl_3 \cdot 9H_2O$, urea, tungstosilicic acid hydrate, methyl orange (MW = 327.33), methyl blue (MW = 799.8), Congo red (MW = 696.66) and Evans blue (MW = 960.79) were bought from Alfa Aesar. Polyacrylonitrile (PAN) support membrane (150,000 Da) was purchased from Shandong Mega Vision Membrane Engineering and Technology Co. Ltd. All chemicals were used without any further treatment or purification.

Preparation of MgAl-SiW_{12} laminates

MgAl-CO_3, MgAl-NO_3 and single-layer MgAl-LDH nanosheets were synthesized in accordance with previously reported methods.[56] MgAl-SiW_{12} laminates were obtained by slow addition of certain amount of aqueous tungstosilicic acid solution (0.1 mg/mL) to the exfoliated MgAl-LDH nanosheets suspension using a peristaltic pump in a nitrogen atmosphere (the mass ratio of MgAl-LDH to SiW_{12} was 0.8:1).

Fabrication of MgAl-SiW_{12} membranes

The PAN support was partially hydrolyzed in NaOH aq (1.5 M) at 50°C for 0.5 h and then neutralized by soaking in deionized water.[57] MgAl-SiW_{12} laminates were sonicated for 20 min to ensure uniform deposition of selective layer. Different volumes of MgAl-SiW_{12} laminate dispersions were filtered by vacuum filtration to obtain membranes with different thicknesses. It is worth noting that the influence on the selectivity influenced by the PAN support can be ignored because of their large pore sizes. The resulting MgAl-SiW_{12} membranes were dried at 25°C for 12 h. MgAl-NO_3 membrane was fabricated by direct filtration of exfoliated LDH nanosheets. All the membranes were immersed in deionized water for 1 h prior to separation measurements.

Characterization

Structural information of the samples was collected on Bruker D8 ADVANCE (Cu Kα source; scan step: 10° min^{-1}; scan range: 3–70°). The samples were characterized by Fourier transform infrared spectroscopy (Nicolet 8700) and X-ray photoelectron spectroscopy (AXIS Supra). Morphological measurements of the nanosheets were examined by high-resolution transmission electron microscopy (200 kV, JEM-2100) and atomic force microscope (AFM) instrument in a tapping mode (DMFASTSCAN2-SYS). The charge property and particle size distribution of LDH nanosheets and POMs were measured using Malvern Zetasizer Nano ZS90 analyzer. The surface potentials of membranes were measured by solid surface zeta potential analyzer (Anton Paar GmbH). ICP-OES analysis was performed on an Agilent 725ES instrument. Solid-state NMR studies were carried out using a Bruker Advance 300M solid-state spectrometer. Morphologies of the MgAl-SiW_{12} membranes were characterized by scanning electron microscopy (SEM) (20 kV, Zeiss Supra 55). The photoluminescence spectra were carried out on a spectrophotometer (F-7000 FL). The UV-vis adsorption spectra were analyzed in the range of 200–800 nm using a Shimadzu UV2600 spectrophotometer. Brunauer-Emmett-Teller surface areas were collected at 77 K on ASAP-2460-4N. Electrochemical impedance spectroscopy (EIS) (scanning frequency: 100 kHz–0.01 Hz; electrolyte: 100 mM, pH 7.0, Na_2SO_4 solution) and photocurrent data (light source: Xe lamp, 300 W; electrolyte: 100 mM, pH 7.0, Na_2SO_4 solution) were obtained on an electrochemical workstation (CHI 760E). Electron spin resonance (ESR) spectroscopy was monitored by Bruker EMX-500 spectrometer. A 300 W Xe lamp was used to irradiate the samples for 10 min at room temperature (298 K) in the presence of 5, 5-dimethyl-1-pyrroline N-oxide (DMPO) to trap the free radicals generated upon irradiation. A low-field nuclear magnetic resonance apparatus was used to analyze the nanoconfined space of the formed membrane (MesoMR23-060H-I; Suzhou Niumag Corporation).

SUPPLEMENTAL INFORMATION

Supplemental information can be found online at https://doi.org/10.1016/j.xcrp.2022.101189.

ACKNOWLEDGMENTS

This research was supported by the National Nature Science Foundation of China (22178019, 22208013, 22288102) and the Fundamental Research Funds for the Central Universities (XK1802-6, XK1803-05, XK1902). H.N.M. would like to thank the University of Glasgow for supporting this work.

AUTHOR CONTRIBUTIONS

W.-L.Z., W.C., H.N.M., and Y.-F.S. conceived the idea, designed the experiment process, and wrote the manuscript. Y.L. finished the theoretical simulation. W.-L.Z. finished the experiment and performed the characterization of the membrane performance and materials preparation with the help of Y.Y.

DECLARATION OF INTERESTS

The authors declare no competing interests.

Received: August 29, 2022
Revised: October 21, 2022
Accepted: November 18, 2022
Published: December 9, 2022

REFERENCES

1. Marchetti, P., Jimenez Solomon, M.F., Szekely, G., and Livingston, A.G. (2014). Molecular separation with organic solvent nanofiltration: a critical review. Chem. Rev. *114*, 10735–10806.

2. Chen, L., Shi, G., Shen, J., Peng, B., Zhang, B., Wang, Y., Bian, F., Wang, J., Li, D., Qian, Z., et al. (2017). Ion sieving in graphene oxide membranes via cationic control of interlayer spacing. Nature *550*, 380–383.

3. Dou, H., Jiang, B., Xu, M., Zhang, Z., Wen, G., Peng, F., Yu, A., Bai, Z., Sun, Y., Zhang, L., et al. (2019). Boron nitride membranes with a distinct nanoconfinement effect for efficient ethylene/ethane separation. Angew. Chem. Int. Ed. Engl. *58*, 13969–13975.

4. Di, M., Hu, L., Gao, L., Yan, X., Zheng, W., Dai, Y., Jiang, X., Wu, X., and He, G. (2020). Covalent organic framework (COF) constructed proton permselective membranes for acid supporting redox flow batteries. Chem. Eng. J. *399*, 125833.

5. Guo, Z., Jiang, H., Wu, H., Zhang, L., Song, S., Chen, Y., Zheng, C., Ren, Y., Zhao, R., Li, Y., et al. (2021). Oil-water-oil triphase synthesis of Ionic covalent organic framework nanosheets. Angew. Chem. Int. Ed. Engl. *60*, 27078–27085.

6. Wu, M., Jiang, X., Meng, Y., Niu, Y., Yuan, Z., Du, S., Li, X., Ruan, X., Xiao, W., Yan, X., and He, G. (2022). A covalent organic framework membrane with homo hierarchical pores for confined reactive crystallization. ACS Appl. Mater. Interfaces *14*, 4739–4749.

7. Wu, X., Cui, X., Wu, W., Wang, J., Li, Y., and Jiang, Z. (2019). Elucidating ultrafast molecular permeation through well-defined 2D nanochannels of lamellar membranes. Angew. Chem. Int. Ed. Engl. *58*, 18524–18529.

8. Ding, L., Li, L., Liu, Y., Wu, Y., Lu, Z., Deng, J., Wei, Y., Caro, J., and Wang, H. (2020). Effective ion sieving with $Ti_3C_2T_x$ MXene membranes for production of drinking water from seawater. Nat. Sustain. *3*, 296–302.

9. Bian, Q., Zhang, M., Liu, Y., Liu, L., Li, Y., Wang, C., He, G., and Liu, Y. (2022). Layered double hydroxide-assisted fabrication of prussian blue membranes for precise molecular sieving. Angew. Chem. Int. Ed. Engl. *61*. e202113662.

10. Wang, N., Huang, Z., Li, X., Li, J., Ji, S., and An, Q.-F. (2018). Tuning molecular sieving channels of layered double hydroxides membrane with direct intercalation of amino acids. J. Mater. Chem. A *6*, 17148–17155.

11. Zhang, M., Guan, K., Ji, Y., Liu, G., Jin, W., and Xu, N. (2019). Controllable ion transport by surface-charged graphene oxide membrane. Nat. Commun. *10*, 1253.

12. Zhu, J., Wang, L., Wang, J., Wang, F., Tian, M., Zheng, S., Shao, N., Wang, L., and He, M. (2020). Precisely tunable ion sieving with an Al_{13}-$Ti_3C_2T_x$ lamellar membrane by controlling interlayer spacing. ACS Nano *14*, 15306–15316.

13. Yang, Y., Yang, X., Liang, L., Gao, Y., Cheng, H., Li, X., Zou, M., Ma, R., Yuan, Q., Duan, X., et al. (2019). Large-area graphene-nanomesh/carbon-nanotube hybrid membranes for ionic and molecular nanofiltration. Science *364*, 1057–1062.

14. Ang, E.H., and Chew, J.W. (2019). Two-dimensional transition-metal dichalcogenide-based membrane for ultrafast solvent permeation. Chem. Mater. *31*, 10002–10007.

15. Lu, P., Liu, Y., Zhou, T., Wang, Q., and Li, Y. (2018). Recent advances in layered double hydroxides (LDHs) as two-dimensional membrane materials for gas and liquid separations. J. Membr. Sci. *567*, 89–103.

16. Cheng, Y., Li, L., He, W., Chen, W., Deng, G., and Song, Y.-F. (2020). Seeds embedded epitaxial growth strategy for PAN@LDH membrane with Mortise-Tenon structure as efficient adsorbent for particulate matter capture. Appl. Catal. B Environ. *263*, 118312.

17. Ma, L., Zhou, H., Xu, M., Hao, P., Kong, X., and Duan, H. (2021). Integrating hydrogen production with anodic selective oxidation of sulfides over a CoFe layered double hydroxide electrode. Chem. Sci. *12*, 938–945.

18. Xu, X., Wang, J., Zhou, A., Dong, S., Shi, K., Li, B., Han, J., and O'Hare, D. (2021). High-efficiency CO_2 separation using hybrid LDH-polymer membranes. Nat. Commun. *12*, 3069.

19. Kong, X., Ge, R., Liu, T., Xu, S., Hao, P., Zhao, X., Li, Z., Lei, X., and Duan, H. (2021). Super-stable mineralization of cadmium by calcium-aluminum layered double hydroxide and its large-scale application in agriculture soil remediation. Chem. Eng. J. *407*, 127178.

20. Cronin, L., and Müller, A. (2012). From serendipity to design of polyoxometalates at the nanoscale, aesthetic beauty and applications. Chem. Soc. Rev. *41*, 7333–7334.

21. Hill, C.L. (1998). Introduction: polyoxometalates-multicomponent molecular vehicles to probe fundamental issues and practical problems. Chem. Rev. *98*, 1–2.

22. Misra, A., Kozma, K., Streb, C., and Nyman, M. (2020). Beyond charge balance: counter-cations in polyoxometalate chemistry. Angew. Chem. Int. Ed. Engl. *59*, 596–612.

23. Misra, A., Zambrzycki, C., Kloker, G., Kotyrba, A., Anjass, M.H., Franco Castillo, I., Mitchell, S.G., Güttel, R., and Streb, C. (2020). Water purification and microplastics removal using magnetic polyoxometalate-supported ionic liquid phases (magPOM-SILPs). Angew. Chem. Int. Ed. Engl. *59*, 1601–1605.

24. Li, X.-X., Wang, Y.-X., Wang, R.-H., Cui, C.-Y., Tian, C.-B., and Yang, G.-Y. (2016). Designed assembly of heterometallic cluster organic frameworks based on Anderson-type polyoxometalate clusters. Angew. Chem. Int. Ed. Engl. *55*, 6462–6466.

25. Zheng, S.-T., Zhang, J., and Yang, G.-Y. (2008). Designed synthesis of POM-organic frameworks from $\{Ni_6PW_9\}$ building blocks under hydrothermal conditions. Angew. Chem. Int. Ed. Engl. *47*, 3909–3913.

26. Li, J., Li, D., Xie, J., Liu, Y., Guo, Z., Wang, Q., Lyu, Y., Zhou, Y., and Wang, J. (2016). Pyrazinium polyoxometalate tetrakaidecahedron-like crystals esterify oleic acid with equimolar methanol at room temperature. J. Catal. *339*, 123–134.

27. Wang, Q., Hou, W., Meng, T., Hou, Q., Zhou, Y., and Wang, J. (2019). Direct synthesis of 2, 5-diformylfuran from carbohydrates via carbonizing polyoxometalate based mesoporous poly(ionic liquid). Catal. Today *319*, 57–65.

28. Cherevan, A.S., Nandan, S.P., Roger, I., Liu, R., Streb, C., and Eder, D. (2020). Polyoxometalates on functional substrates: concepts, synergies, and future perspectives. Adv. Sci. *7*. 1903511.

29. Zhao, S., Xu, J., Wei, M., and Song, Y.-F. (2011). Synergistic catalysis by polyoxometalate-intercalated layered double hydroxides: oximation of aromatic aldehydes with large enhancement of selectivity. Green Chem. *13*, 384–389.

30. Li, T., Wang, Z., Chen, W., Miras, H.N., and Song, Y.-F. (2017). Rational design of a polyoxometalate intercalated layered double hydroxide: highly efficient catalytic epoxidation of allylic alcohols under mild and solvent-free conditions. Chem. Eur. J. *23*, 1069–1077.

31. Chen, Y., Yao, Z., Miras, H.N., and Song, Y.-F. (2015). Modular polyoxometalate-layered double hydroxide composites as efficient oxidative catalysts. Chem. Eur. J. *21*, 10812–10820.

32. Chang, W., Qi, B., and Song, Y.-F. (2020). Step-by-step assembly of 2D confined chiral space endowing achiral clusters with asymmetric catalytic activity for epoxidation of allylic alcohols. ACS Appl. Mater. Interfaces *12*, 36389–36397.

33. Li, Z., Zhang, J., Jing, X., Dong, J., Liu, H., Lv, H., Chi, Y., and Hu, C. (2021). A polyoxometalate@covalent triazine framework as a robust electrocatalyst for selective benzyl alcohol oxidation coupled with hydrogen production. J. Mater. Chem. A *9*, 6152–6159.

34. Zhao, X., Duan, Y., Yang, F., Wei, W., Xu, Y., and Hu, C. (2017). Efficient mechanochemical synthesis of polyoxometalate⊂ZIF Complexes as reusable catalysts for highly selective oxidation. Inorg. Chem. *56*, 14506–14512.

35. Dong, J., Lv, H., Sun, X., Wang, Y., Ni, Y., Zou, B., et al. (2018). A versatile self-detoxifying material based on immobilized polyoxoniobate for decontamination of chemical warfare agent simulants. Chem. Eur. J. *24*, 19208–19215.

36. Yang, X., Zhao, H., Feng, J., Chen, Y., Gao, S., and Cao, R. (2017). Visible-light-driven selective oxidation of alcohols using a dye-sensitized TiO_2-polyoxometalate catalyst. J. Catal. *351*, 59–66.

37. Liu, Y., Luo, F., Liu, S., Liu, S., Lai, X., Li, X., Lu, Y., Li, Y., Hu, C., Shi, Z., and Zheng, Z. (2017). Aminated graphene oxide impregnated with photocatalytic polyoxometalate for efficient adsorption of dye pollutants and its facile and complete photoregeneration. Small *13*. 1603174.

38. Wu, L., An, S., and Song, Y.-F. (2021). Heteropolyacids-immobilized graphitic carbon nitride: highly efficient photo-oxidation of

benzyl alcohol in the aqueous phase. Engineering *7*, 94–102.

39. Lu, X., Sakai, N., Tang, D., Li, X., Taniguchi, T., Ma, R., and Sasaki, T. (2020). CoNiFe layered double hydroxide/$RuO_{2.1}$ nanosheet superlattice as carbon-free electrocatalysts for water splitting and Li-O_2 batteries. ACS Appl. Mater. Interfaces *12*, 33083–33093.

40. Ma, D., Liang, L., Chen, W., Liu, H., and Song, Y.-F. (2013). Covalently tethered polyoxometalate-pyrene hybrids for noncovalent sidewall functionalization of single-walled carbon nanotubes as high-performance anode material. Adv. Funct. Mater. *23*, 6100–6105.

41. Cai, Y., Song, H., An, Z., Xiang, X., Shu, X., and He, J. (2018). The confined space electron transfer in phosphotungstate intercalated ZnAl-LDHs enhances its photocatalytic performance for oxidation/extraction desulfurization of model oil in air. Green Chem. *20*, 5509–5519.

42. Zhao, S., Jia, Y., and Song, Y.-F. (2014). Acetalization of aldehydes and ketones over $H_4[SiW_{12}O_{40}]$ and $H_4[SiW_{12}O_{40}]/SiO_2$. Catal. Sci. Technol. *4*, 2618–2625.

43. Zhao, S., Zhu, H., Wang, Z., Song, P., Ban, M., and Song, X. (2018). A loose hybrid nanofiltration membrane fabricated via chelating-assisted in-situ growth of Co/Ni LDHs for dye wastewater treatment. Chem. Eng. J. *353*, 460–471.

44. Yang, L., Yang, H., Wu, H., Zhang, L., Ma, H., Liu, Y., Wu, Y., Ren, Y., Wu, X., and Jiang, Z. (2021). COF membranes with uniform and exchangeable facilitated transport carriers for efficient carbon capture. J. Mater. Chem. A *9*, 12636–12643.

45. Lv, Y., Zhang, C., He, A., Yang, S.-J., Wu, G.-P., Darling, S., and Xu, Z.-K. (2017). Photocatalytic nanofiltration membranes with self-cleaning property for wastewater treatment. Adv. Funct. Mater. *27*. 1700251.

46. Liu, Y., Wu, H., Min, L., Song, S., Yang, L., Ren, Y., et al. (2020). 2D layered double hydroxide membranes with intrinsic breathing effect toward CO_2 for efficient carbon capture. J. Membr. Sci. *598*, 117663.

47. Jia, Y., Fang, Y., Zhang, Y., Miras, H.N., and Song, Y.-F. (2015). Classical keggin intercalated into layered double hydroxides: facile preparation and catalytic efficiency in knoevenagel condensation reactions. Chem. Eur. J. *21*, 14862–14870.

48. Zhang, W.-H., Yin, M.-J., Zhao, Q., Jin, C.-G., Wang, N., Ji, S., Ritt, C.L., Elimelech, M., and An, Q.-F. (2021). Graphene oxide membranes with stable porous structure for ultrafast water transport. Nat. Nanotechnol. *16*, 337–343.

49. Li, X., Wang, Y., Chang, J., Sun, H., He, H., Qian, C., Kheirabad, A.K., An, Q.-F., Wang, N., Zhang, M., and Yuan, J. (2021). "Mix-then-on-demand-complex": in situ cascade anionization and complexation of graphene oxide for high-performance nanofiltration membranes. ACS Nano *15*, 4440–4449.

50. Bai, S., Wang, Z., Tan, L., Waterhouse, G.I.N., Zhao, Y., and Song, Y.-F. (2020). 600 nm irradiation-induced efficient photocatalytic CO_2 reduction by ultrathin layered double hydroxide nanosheets. Ind. Eng. Chem. Res. *59*, 5848–5857.

51. Tan, L., Xu, S.-M., Wang, Z., Xu, Y., Wang, X., Hao, X., Bai, S., Ning, C., Wang, Y., Zhang, W., et al. (2019). Highly selective photoreduction of CO_2 with suppressing H_2 evolution over monolayer layered double hydroxide under irradiation above 600 nm. Angew. Chem. Int. Ed. Engl. *58*, 11860–11867.

52. Ning, C., Wang, Z., Bai, S., Tan, L., Dong, H., Xu, Y., Hao, X., Shen, T., Zhao, J., Zhao, P., et al. (2021). 650 nm-driven syngas evolution from photocatalytic CO_2 reduction over Co-containing ternary layered double hydroxide nanosheets. Chem. Eng. J. *412*, 128362.

53. Huang, X., Xu, X., Yang, R., and Fu, X. (2022). Synergetic adsorption and photocatalysis performance of g-C_3N_4/Ce-doped MgAl-LDH in degradation of organic dye under LED visible light. Colloids Surf. A Physicochem. Eng. Asp. *643*, 128738.

54. Li, J., Xu, Y., Ding, Z., Mahadi, A.H., Zhao, Y., and Song, Y.-F. (2020). Photocatalytic selective oxidation of benzene to phenol in water over layered double hydroxide: a thermodynamic and kinetic perspective. Chem. Eng. J. *388*, 124248.

55. Meng, J., Wang, X., Yang, X., Hu, A., Guo, Y., and Yang, Y. (2019). Enhanced gas-phase photocatalytic removal of aromatics over direct Z-scheme-dictated $H_3PW_{12}O_{40}$/g-C_3N_4 film-coated optical fibers. Appl. Catal. B Environ. *251*, 168–180.

56. Jia, Y., Zhao, S., and Song, Y.-F. (2014). The application of spontaneous flocculation for the preparation of lanthanide-containing polyoxometalates intercalated layered double hydroxides: highly efficient heterogeneous catalysts for cyanosilylation. Appl. Catal. A Gen. *487*, 172–180.

57. Li, W., Yang, Z., Zhang, G., Fan, Z., Meng, Q., Shen, C., and Gao, C. (2014). Stiff metal–organic framework–polyacrylonitrile hollow fiber composite membranes with high gas permeability. J. Mater. Chem. A *2*, 2110–2118.